AGU PUBLICATIONS

JGR

Journal of Geophysical Research: Atmospheres

RESEARCH ARTICLE
10.1002/2013JD020188

**Key Points:**
- OMI AOD is comparable with AERONET, MODIS Deep Blue, and MISR AOD values
- Adequate sensitivity of UV remote sensing to aerosols in the boundary layer

**Correspondence to:**
C. Ahn,
Changwoo.Ahn@ssaihq.com

**Citation:**
Ahn, C., O. Torres, and H. Jethva (2014), Assessment of OMI near-UV aerosol optical depth over land, *J. Geophys. Res. Atmos.*, *119*, 2457–2473, doi:10.1002/2013JD020188.

Received 23 MAY 2013
Accepted 18 JAN 2014
Accepted article online 23 JAN 2014
Published online 7 MAR 2014



# Assessment of OMI near-UV aerosol optical depth over land

**Changwoo Ahn[1], Omar Torres[2], and Hiren Jethva[3]**

[1]Science Systems and Applications, Inc., Lanham, Maryland, USA, [2]NASA Goddard Space Flight Center, Greenbelt, Maryland, USA, [3]Universities Space Research Association, Columbia, Maryland, USA

**Abstract** This is the first comprehensive assessment of the aerosol optical depth (AOD) product retrieved from the near-UV observations by the Ozone Monitoring Instrument (OMI) onboard the Aura satellite. The OMI-retrieved AOD by the UV aerosol algorithm (OMAERUV version 1.4.2) was evaluated using collocated Aerosol Robotic Network (AERONET) level 2.0 direct Sun AOD measurements over 8 years (2005–2012). A time series analysis of collocated satellite and ground-based AOD observations over 8 years shows no discernible drift in OMI's calibration. A rigorous validation analysis over 4 years (2005–2008) was carried out at 44 globally distributed AERONET land sites. The chosen locations are representative of major aerosol types such as smoke from biomass burning or wildfires, desert mineral dust, and urban/industrial pollutants. Correlation coefficient ($\rho$) values of 0.75 or better were obtained at 50% of the sites with about 33% of the sites in the analysis reporting regression line slope values larger than 0.70 but always less than unity. The combined AERONET-OMAERUV analysis of the 44 sites yielded a $\rho$ of 0.81, slope of 0.79, $y$ intercept of 0.10, and 65% OMAERUV AOD falling within the expected uncertainty range (largest of 30% or 0.1) at 440 nm. The most accurate OMAERUV retrievals are reported over northern Africa locations where the predominant aerosol type is desert dust and cloud presence is less frequent. Reliable retrievals were documented at many sites characterized by urban-type aerosols with low to moderate AOD values, concentrated in the boundary layer. These results confirm that the near-UV observations are sensitive to the entire aerosol column. A simultaneous comparison of OMAERUV, Moderate Resolution Imaging Spectroradiometer (MODIS) Deep Blue, and Multiangle Imaging Spectroradiometer (MISR) AOD retrievals to AERONET measurements was also carried out to evaluate the OMAERUV accuracy in relation to those of the standard aerosol satellite products. The outcome of the comparison indicates that OMAERUV, MODIS Deep Blue, and MISR retrieval accuracies in arid and semiarid environments are statistically comparable.

## 1. Introduction

Reliable information of global aerosol optical properties from satellites is critical for climate studies and for the assessment of aerosol transport models. The accurate characterization of the aerosol load is also required for trace gas remote sensing and air quality applications [*Al-Saadi et al.*, 2005; *Kinne et al.*, 2006; *Leitão et al.*, 2010; *Ridley et al.*, 2012; *van Donkelaar et al.*, 2010; *Wang and Christopher*, 2003; *Zhang et al.*, 2008]. Modern spaceborne aerosol sensing instruments such as the Moderate Resolution Imaging Spectroradiometer (MODIS), the Multiangle Imaging Spectroradiometer (MISR), the Polarization and Directionality of the Earth Reflectances (POLDER), and the Cloud-Aerosol Lidar with Orthogonal Polarization (CALIOP) probe the atmosphere with the purpose of characterizing aerosol physical properties and amounts. This is accomplished by the use of multiwavelength (MODIS), multiangle (MISR), and polarization (POLDER) observations and retrieval algorithms. Based on the measurements by these sensors, a great progress has been made over the last decade in the understanding of the global aerosol distribution, aerosol sources, and the impact of atmospheric particulates on the Earth's radiation budget [*Deuzé et al.*, 2001; *Kaufman et al.*, 1997; *Martonchik et al.*, 1998; *Winker et al.*, 2006; *Xu et al.*, 2013; *Zhang and Christopher*, 2003]. With each sensor having its own strengths and limitations when retrieving aerosol properties, multiple sensor observations are highly recommended in order to complement the limitations and increase synergy effects [*King et al.*, 1999; *Schoeberl et al.*, 2006; *Stephens et al.*, 2002]. To this end, the Ozone Monitoring Instrument (OMI) onboard the EOS-Aura satellite, part of the A-train satellite constellation [*Levelt et al.*, 2006; *Stephens et al.*, 2002], has the unique advantage of providing information on aerosol optical properties by making use of the large sensitivity to aerosol absorption in the near-ultraviolet (UV) spectral region. Another important advantage is the

low near-UV surface albedo at all terrestrial surfaces which reduces the error associated with land surface reflectance characterization.

In spite of the $13 \times 24\,km^2$ coarse sensor footprint designed for the monitoring of atmospheric trace gas composition using hyperspectral measurements, the OMI observations in the near UV (354 and 388 nm) can be used to retrieve aerosol optical depth and single-scattering albedo under cloud-free conditions. The OMI aerosol retrieval capability draws on heritage from the Total Ozone Mapping Spectrometer series of instruments [*Torres et al*., 1998, 2002a]. Two aerosol algorithms are applied to the OMI observations: a multiwavelength inversion (OMAERO) and a two near-UV channel (OMAERUV). The OMAERO algorithm, developed and maintained by the Royal Netherlands Meteorological Institute (KNMI), uses a spectral fitting method described by *Torres et al*. [2007]. The OMAERUV algorithm produces the absorbing aerosol index, aerosol extinction optical depth (AOD), aerosol absorption optical depth (AAOD), and single-scattering albedo (SSA) from the observations at 354 and 388 nm [*Torres et al*., 2007, 2013]. The focus of this paper is the assessment of OMAERUV AOD retrievals.

The OMI AOD and SSA retrievals by the initial OMAERUV algorithm have been previously evaluated with AERONET (Aerosol Robotic Network) observations [*Torres et al*., 2007]. The OMI AOD retrievals were also compared to MODIS and MISR observations [*Ahn et al*., 2008] showing agreement in terms of seasonal annual cycles over most of the major emission sources of carbonaceous aerosols from biomass burning and mineral dust from deserts. However, the magnitude of OMI AOD after accounting for differences in reporting wavelength was generally higher than those of MODIS and MISR.

Since those early evaluations, OMI calibration has been updated [*Dobber et al*., 2008], and important algorithm improvements have been implemented in OMAERUV [*Torres et al*., 2013]. The carbonaceous aerosol model was replaced with a new model that accounts for the presence of organic carbon as an important absorbing agent of aerosols generated by biomass burning and wildfires [*Jethva and Torres*, 2011]. Other improvements include the development of a CALIOP-based aerosol layer height climatology and the use of Atmospheric Infrared Sounder carbon monoxide real-time observations to distinguish smoke from dust-type aerosols [*Torres et al*., 2013]. A detailed description of these upgrades and other algorithm modifications is given by *Torres et al*. [2013].

The preliminary evaluations of OMAERUV's performance after these upgrades have been documented. The CALIOP-derived climatology of aerosol layer height improved the retrieval performances in the range of 5–20% [*Torres et al*., 2013] in terms of the expected uncertainty envelope (0.1 or ±30%). A significant improvement in the AOD retrieval performance over South America was reported by *Jethva and Torres* [2011] after accounting for the spectral dependence of carbonaceous aerosol absorption properties in the forward calculations used in the lookup tables.

In this paper, we carry out a more extensive evaluation of OMAERUV AOD by comparing to ground-based observations as well as to other satellite AOD products over land.

The aim of this paper is to document the improvements of the OMAERUV AOD product (version 1.4.2) by direct evaluation using space and time-collocated comparisons to independent AOD data sets such as the Aerosol Robotic Network as well as the Aqua-MODIS Deep Blue (MODIS DB) and Terra-MISR AOD products.

A general description of the data sets in the comparative analysis and a detailed discussion of the spatial and temporal collocation of satellite and ground-based observations are presented in section 2. In section 3, we first examine the OMAERUV AOD record over the full complete 8 years of OMI operation (2005–2012) to assess the long-term stability of the satellite observations. This is done by comparing the daily AOD values from the OMI observations to the AERONET level 2.0 AOD data at five selected sites. A more comprehensive evaluation is then carried out at 44 AERONET sites over 4 years (2005–2008). In section 4, we further assess the OMI AOD retrievals in 2007 over desert areas by comparisons with other satellite products reporting AOD over bright land surfaces including the MODIS DB, MISR, and OMAERO AOD products. This is the first time the two OMI aerosol algorithms are intercompared. All the satellite retrievals in this analysis are independently validated using AERONET observations, and the resulting statistics are intercompared. This intersatellite analysis is carried out primarily over northern Africa including the Saharan desert and Sahel regions where large-scale dust storm and smoke from biomass burning events typically take place under favorable cloud-free conditions. The final section provides a summary of results and discusses future work.

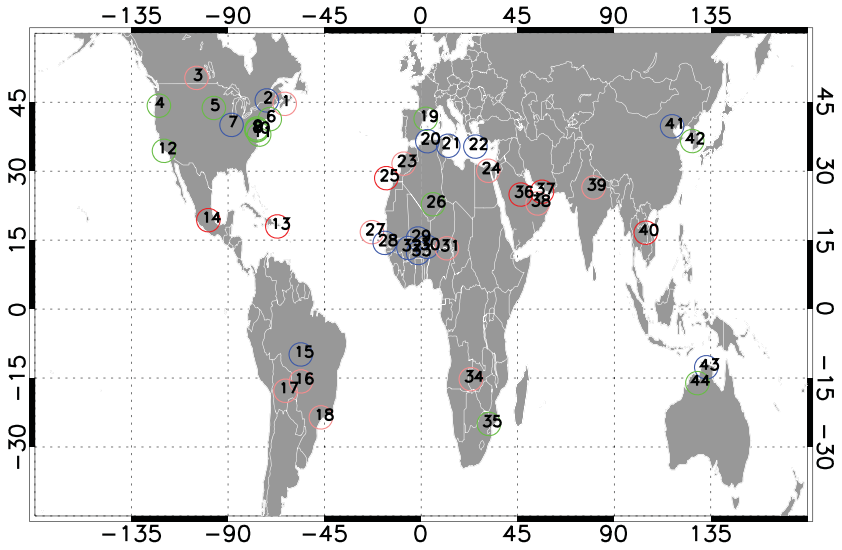


**Figure 1.** Global locations of the selected 44 AERONET sites used for comparisons with OMI AOD. Colors indicate the percent ($Q$) of daily OMI-matched AOD values falling within the uncertainty envelope of ±30% or 0.1 AOD (green circle: $Q \geq 70\%$, blue circle: $60\% \leq Q < 70\%$, pink circle: $50\% \leq Q < 60\%$, and red circle: $Q < 50\%$) in scatterplots (see details in text). The site ID numbers are roughly arranged from the north to the south and from the west to the east directions for convenience. The site names and geolocations for each site ID are shown in Table 1.

## 2. Data Sets and Methodology

### 2.1. OMAERUV Data

The OMAERUV level 2 daily files are available at the Goddard Earth Sciences Data and Information Services Center (GES DISC) site (http://disc.sci.gsfc.nasa.gov/Aura/data-holdings/OMI/omaeruv_v003.shtml). The retrieved values of AOD, AAOD, and SSA are reported at 388 nm. Similar values are also reported at 354 and 500 nm by conversion from the 388 nm retrieval. The wavelength conversions from 388 nm to 354 and 500 nm are done using the spectral dependence associated with the assumed aerosol particle size distribution and retrieved absorption information [*Torres et al*., 2007; *Jethva and Torres*, 2011].

The final quality flag parameter in the OMAERUV level 2 files is a quality assurance (QA) flag that indicates the level of confidence on the retrieved parameters with regard to the interference of subpixel size cloud presence. Best retrievals, i.e., minimally affected by subpixel cloud contamination, have a QA flag of 0 and are deemed suitable for scientific use.

The OMI has undergone an instrumental problem, the so-called "row anomaly," since mid-2007, and this has affected almost half of the 60 rows in a cross-track direction with unpredictable patterns, depending on seasons and latitudes up to present (2013). With our best knowledge, these affected rows have been flagged and filtered out before making comparisons in this study. A more detailed description of the OMI row anomaly is available at http://www.knmi.nl/omi/research/product/rowanomaly-background.php

### 2.2. AERONET Data

The AERONET project [*Holben et al*., 1998] is a robotic network of globally distributed ground-based Cimel Sun photometers. The sensors are automatically operated to measure solar irradiance and sky radiances in order to provide quality-assured aerosol optical properties needed for validation of satellite retrievals and assessment of model calculations. Standard AODs from the direct Sun measurements are available nominally at 340, 380, 440, 500, 675, 870, and 1020 nm. The calibration of the AERONET Sun photometers is maintained regularly by comparing the well-calibrated reference Cimel instruments at the Goddard Space Flight Center with the Langley method used at the Mauna Loa Observatory in Hawaii.

### 2.3. Other Satellite Data Sets

MISR measures the upwelling short-wave radiance at the top of the atmosphere in four spectral bands centered at 446, 558, 672, and 866 nm. Measurements are obtained at each of nine view angles along the

**Table 1.** Information of the Selected 44 AERONET Sites[a]

| Site No. | Site Name | Longitude | Latitude | Elevation (m) | Wavelength (nm) | Aerosol Type |
|---|---|---|---|---|---|---|
| 1 | Halifax | 63.594°W | 44.638°N | 65 | 380 | nonabsorbing |
| 2 | Centre d'Applications et de Recherches en Télédétection | 71.931°W | 45.379°N | 300 | 380 | nonabsorbing |
| 3 | Bratt's Lake | 104.700°W | 50.280°N | 586 | 380 | nonabsorbing |
| 4 | HJ Andrews | 122.224°W | 44.239°N | 830 | 440 | nonabsorbing |
| 5 | Sioux Falls | 96.626°W | 43.736°N | 500 | 380 | nonabsorbing |
| 6 | Martha's Vineyard Coastal Observatory | 70.550° W | 41.300° N | 10 | 440 | nonabsorbing |
| 7 | Bondville | 88.372°W | 40.053°N | 212 | 380 | nonabsorbing |
| 8 | GSFC | 76.840°W | 38.992°N | 87 | 380 | nonabsorbing |
| 9 | Maryland Science Center | 76.617°W | 39.283°N | 15 | 380 | nonabsorbing |
| 10 | SERC | 76.500°W | 38.883°N | 10 | 380 | nonabsorbing |
| 11 | Wallops | 75.475°W | 37.942°N | 10 | 440 | nonabsorbing |
| 12 | UCSB | 119.845° W | 34.415° N | 33 | 380 | nonabsorbing |
| 13 | La Parguera | 67.045°W | 17.970°N | 12 | 380 | nonabsorbing |
| 14 | Mexico City | 99.182°W | 19.334°N | 2263 | 380 | nonabsorbing |
| 15 | Alta Floresta | 56.104°W | 9.871°S | 277 | 380 | mixture |
| 16 | Cuiaba, Miranda | 56.021°W | 15.729°S | 210 | 380 | nonabsorbing |
| 17 | Santa Cruz, Universidad Tecnológica Privada de Santa Cruz | 63.201°W | 17.767°S | 432 | 440 | nonabsorbing |
| 18 | Sao Paulo | 46.735°W | 23.561°S | 865 | 380 | nonabsorbing |
| 19 | Barcelona | 2.117°E | 41.386°N | 125 | 440 | nonabsorbing |
| 20 | Blida | 2.881°E | 36.508°N | 230 | 380 | nonabsorbing |
| 21 | Lampedusa | 12.632°E | 35.517°N | 45 | 440 | dust |
| 22 | Foundation for Research and Technology-Hellas, Crete | 25.282°E | 35.333°N | 20 | 380 | nonabsorbing |
| 23 | Saada | 8.156°W | 31.626°N | 420 | 440 | dust |
| 24 | Cairo, Egyptian Meteorological Authority | 31.290°W | 30.081°N | 70 | 440 | dust |
| 25 | Santa Cruz Tenerife | 16.247°W | 28.473°N | 52 | 380 | mixture |
| 26 | Tamanrasset | 5.530°E | 22.790°N | 1377 | 440 | dust |
| 27 | Capo Verde | 22.935°W | 16.733°N | 60 | 440 | dust |
| 28 | Dakar | 16.959°W | 14.394°N | 0 | 440 | dust |
| 29 | Agoufou | 1.479°W | 15.345°N | 305 | 440 | mixture |
| 30 | Banizoumbou | 2.665°E | 13.541°N | 250 | 440 | smoke |
| 31 | DMN Maine Soroa | 12.023°E | 13.217°N | 350 | 440 | smoke |
| 32 | IER, Cinzana | 5.934°W | 13.278°N | 285 | 440 | smoke |
| 33 | Ouagadougou | 1.400°W | 12.200°N | 290 | 440 | smoke |
| 34 | Mongu | 23.151°E | 15.254°S | 1107 | 380 | mixture |
| 35 | Skukuza | 31.587°E | 24.992°S | 150 | 380 | nonabsorbing |
| 36 | Solar Village | 46.397°E | 24.907°N | 764 | 380 | dust |
| 37 | Dhadnah | 56.325°E | 25.513°N | 81 | 380 | dust |
| 38 | Hamim | 54.300°E | 22.967°N | 209 | 380 | dust |
| 39 | Kanpur | 80.232°E | 26.513°N | 123 | 380 | mixture |
| 40 | Mukdahan | 104.676°E | 16.607°N | 166 | 380 | smoke |
| 41 | XiangHe | 116.962°E | 39.754°N | 36 | 380 | smoke |
| 42 | Anmyon | 126.330°E | 36.539°N | 47 | 380 | smoke |
| 43 | Jabiru | 132.893°E | 12.661°S | 30 | 380 | nonabsorbing |
| 44 | Lake Argyle | 128.749°E | 16.108°S | 150 | 380 | dust |

[a]Predominant aerosol types are determined by the OMAERUV (see details in text).

flight path, at ±70.5°, ±60.0°, ±45.6°, ±26.1°, and nadir. These views allow the algorithm to retrieve aerosol properties over bright desert surfaces by distinguishing surface from atmospheric contributions to the top-of-atmosphere [*Diner et al*., 2005; *Kahn et al*., 2010].

The MODIS Deep Blue algorithm [*Hsu et al*., 2004] takes advantage of the dark surface reflectance at blue channels (412 and 470 nm) and the weak absorption of dust at the red channel (650 nm). The algorithm is

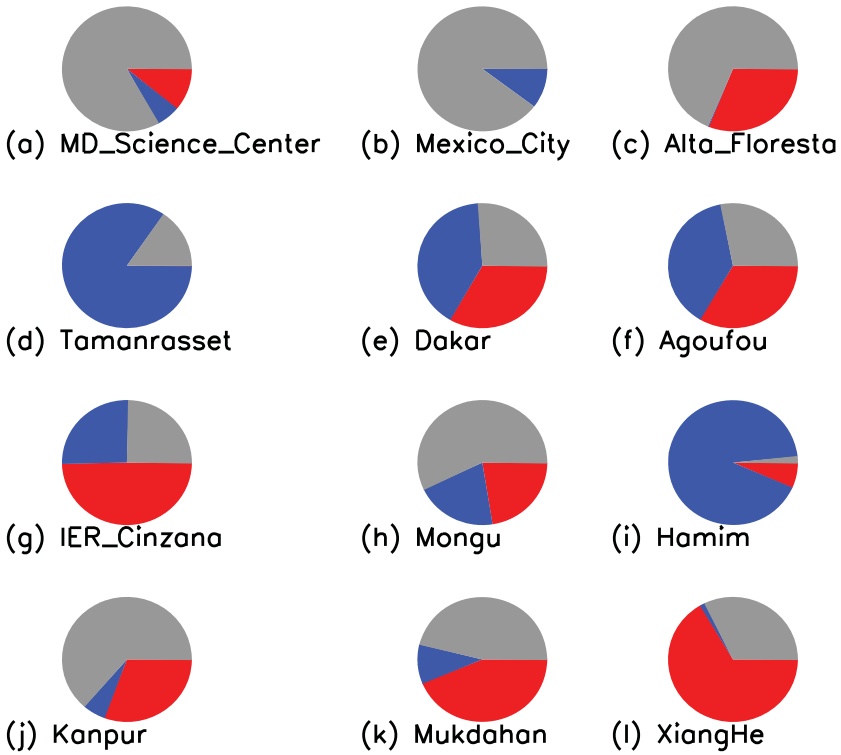


**Figure 2.** Pie charts of three aerosol types identified from the OMI overpass data at the selected 12 AERONET sites for 4 years (2005–2008). Each aerosol type is shown as red (smoke), blue (dust), and gray color (nonabsorbing aerosols).

especially designed to provide AOD over the bright surfaces including desert areas for which the MODIS standard dark land target aerosol algorithm fails to retrieve reliable aerosol products [*Kaufman et al*., 1997; *Chu et al*., 2002; *Levy et al*., 2010]. With enough cross-track swath coverage (2330 km) comparable to that of OMI (2600 km), this product is useful for comparison with OMI AOD, especially over desert areas where not only the most intense dust storms usually take place but have limited observations and retrievals.

The OMAERO multiwavelength algorithm is based on the spectral information in the near UV and the visible of 14 wavelength bands, which are about 1 nm wide and are located at 342.5, 367.0, 376.5, 388.0, 399.5, 406.0, 416.0, 425.5, 436.5, 442.0, 451.5, 463.0, and 477.0 nm. The precision in the retrieved AOD is given in terms of the retrieval error of the nonlinear fitting routine; the QA flags however are not provided (OMAERO Readme file available at http://disc.sci.gsfc.nasa.gov/Aura/data-holdings/OMI/omaero_v003.shtml). The OMAERO algorithm uses no external constraints on aerosol plume height and aerosol type. The derived spectral aerosol optical depth however depends strongly on these parameters which are provided with the best fitting aerosol type [*Torres et al*., 2007].

Level 2 files and related documents for AOD products from other satellite-borne sensors are available from the NASA data centers as follows: the level 1 and Atmosphere Archive and Distribution System site (http://ladsweb.nascom.nasa.gov/data/search.html) for the Aqua/MODIS Deep Blue AOD product (collection 5.1; MYD04_L2), designated as MODIS DB in this study, the Langley Atmospheric Science Data Center site (http://eosweb.larc.nasa.gov/PRODOCS/misr/table_misr.html) for the Terra MISR AOD product (version 22), and the GES DISC (http://disc.sci.gsfc.nasa.gov/Aura/data-holdings/OMI/omaero_v003.shtml) for the OMAERO AOD product version 1.2.3.1.

### 2.4. OMAERUV-AERONET Collocation

The OMI AOD values with a QA flag of 0 were collocated in space and time with AERONET version 2.0 level 2.0 (cloud screened and calibrated) direct Sun measurements. The comparative analysis was carried over a 4 year period from 2005 to 2008 at the 44 AERONET sites. These locations and detailed information of the sites are in Figure 1 and Table 1.

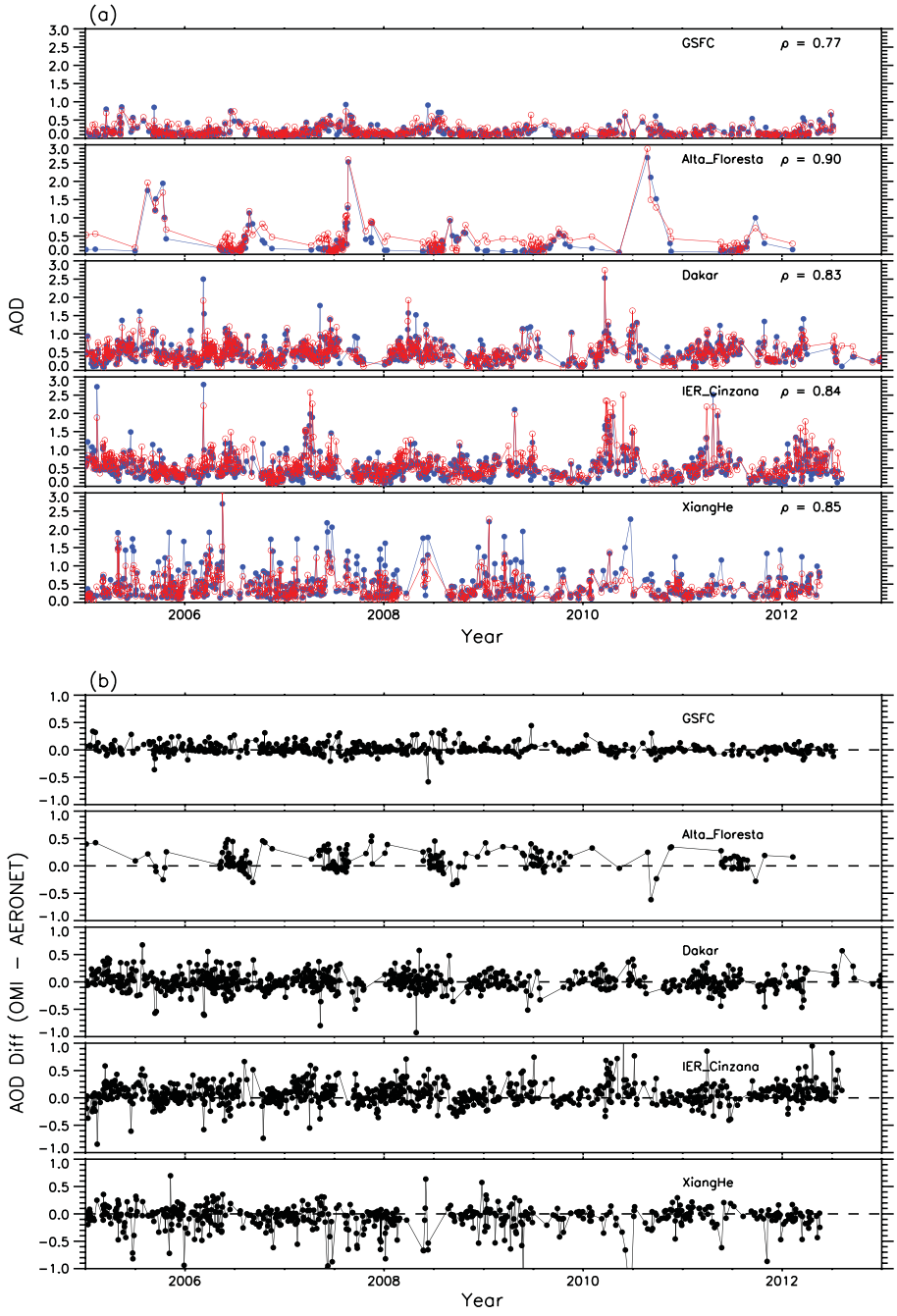


**Figure 3.** (a) AOD time series plot over the five sites for 8 years (2005–2012). Red open circles are daily OMI AOD values corresponding to those from AERONET (blue solid circles). (b) Time series of AOD differences (OMI-AERONET) for 8 years (2005–2012).

The site selection criteria take into account the regionally dominant aerosol type as well as the availability of multiyear records. This will adequately evaluate the algorithm capability of capturing both the seasonal and interannual variability. The predominant aerosol type in Table 1 was determined from the statistics of the three aerosol types (i.e., smoke, dust, and urban/industrial) used in OMAERUV [*Torres et al.*, 2007]. Examples of the observed statistics are shown in Figure 2 for some of the selected sites. The occurrence of absorbing aerosols (i.e., dust and smoke) is generally seasonal. The predominant aerosol type is determined based on the following criteria: (i) nonabsorbing aerosol site when urban/industrial aerosols are present over 70% of the time and (ii) dust or smoke sites when either dust or smoke has a frequency of occurrence larger than 40%. All other instances of aerosol occurrence are labeled as a mixture in Table 1.

**Table 2.** Summary Statistics of OMI AOD Versus AERONET AOD Over 4 Years (2005–2008)[a]

| Site No. | *N* | avg ± (SE) | SDEV2 | SDEV1 | *Q* | RMSE | *y* intercept | Slope | $\rho$ |
|---|---|---|---|---|---|---|---|---|---|
| | | | | (a) Sites with 380 nm | | | | | |
| 35 | 338 | 0.08 (0.01) | 0.12 | 0.20 | 80.18 | 0.11 | 0.08 | 0.74 | 0.82 |
| 10 | 132 | 0.06 (0.01) | 0.10 | 0.15 | 80.3 | 0.09 | 0.04 | 0.80 | 0.80 |
| 20 | 326 | 0.11 (0.01) | 0.12 | 0.20 | 60.74 | 0.11 | 0.01 | 0.73 | 0.79 |
| 9 | 234 | 0.06 (0.01) | 0.09 | 0.13 | 83.33 | 0.08 | 0.04 | 0.83 | 0.79 |
| 8 | 294 | 0.07 (0.01) | 0.10 | 0.15 | 81.3 | 0.09 | 0.06 | 0.73 | 0.77 |
| 39 | 193 | 0.21 (0.02) | 0.25 | 0.32 | 53.37 | 0.25 | 0.01 | 0.85 | 0.75 |
| 15 | 106 | 0.15 (0.02) | 0.18 | 0.42 | 61.32 | 0.17 | 0.12 | 0.92 | 0.91 |
| 41 | 314 | 0.15 (0.01) | 0.22 | 0.45 | 65.61 | 0.17 | 0.09 | 0.67 | 0.87 |
| 16 | 161 | 0.15 (0.02) | 0.22 | 0.37 | 57.76 | 0.16 | 0.12 | 0.59 | 0.80 |
| 40 | 133 | 0.20 (0.02) | 0.23 | 0.36 | 49.62 | 0.16 | 0.13 | 0.52 | 0.78 |
| 42 | 71 | 0.15 (0.03) | 0.24 | 0.36 | 71.83 | 0.17 | 0.14 | 0.54 | 0.75 |
| 34 | 146 | 0.14 (0.02) | 0.21 | 0.30 | 56.16 | 0.15 | 0.10 | 0.55 | 0.74 |
| 44 | 543 | 0.08 (0.01) | 0.11 | 0.14 | 78.64 | 0.11 | 0.07 | 0.75 | 0.70 |
| 12 | 205 | 0.07 (0.01) | 0.10 | 0.13 | 73.66 | 0.09 | 0.08 | 0.61 | 0.68 |
| 1 | 158 | 0.11 (0.01) | 0.12 | 0.12 | 59.5 | 0.12 | 0.11 | 0.86 | 0.67 |
| 7 | 183 | 0.09 (0.01) | 0.10 | 0.12 | 68.85 | 0.09 | 0.10 | 0.68 | 0.66 |
| 18 | 101 | 0.13 (0.02) | 0.17 | 0.23 | 53.47 | 0.13 | 0.12 | 0.50 | 0.66 |
| 2 | 94 | 0.11 (0.01) | 0.13 | 0.13 | 62.77 | 0.13 | 0.10 | 0.82 | 0.64 |
| 38 | 255 | 0.15 (0.01) | 0.18 | 0.19 | 50.98 | 0.17 | 0.18 | 0.72 | 0.63 |
| 43 | 253 | 0.12 (0.01) | 0.16 | 0.13 | 62.05 | 0.15 | 0.09 | 0.93 | 0.62 |
| 22 | 309 | 0.10 (0.01) | 0.13 | 0.14 | 66.02 | 0.12 | 0.08 | 0.71 | 0.61 |
| 36 | 461 | 0.31 (0.01) | 0.20 | 0.19 | 17.79 | 0.19 | 0.38 | 0.76 | 0.61 |
| 3 | 190 | 0.11 (0.01) | 0.13 | 0.13 | 59.47 | 0.12 | 0.13 | 0.69 | 0.60 |
| 13 | 158 | 0.16 (0.01) | 0.17 | 0.14 | 44.3 | 0.17 | 0.17 | 0.79 | 0.57 |
| 5 | 244 | 0.09 (0.01) | 0.12 | 0.11 | 72.13 | 0.11 | 0.10 | 0.69 | 0.57 |
| 14 | 90 | 0.22 (0.03) | 0.30 | 0.33 | 47.78 | 0.20 | 0.30 | 0.33 | 0.48 |
| 25 | 72 | 0.18 (0.03) | 0.23 | 0.20 | 48.61 | 0.21 | 0.24 | 0.49 | 0.42 |
| 37 | 342 | 0.27 (0.01) | 0.26 | 0.22 | 33.04 | 0.24 | 0.45 | 0.48 | 0.41 |
| Total | 6106 | 0.05 (0.003) | 0.20 | 0.27 | 60.74 | 0.18 | 0.12 | 0.73 | 0.73 |
| | | | | (b) Sites with 440 nm | | | | | |
| 26 | 401 | 0.08 (0.01) | 0.09 | 0.2 | 73.07 | 0.08 | 0.08 | 0.76 | 0.88 |
| 11 | 294 | 0.06 (0.00) | 0.08 | 0.14 | 88.10 | 0.07 | 0.04 | 0.73 | 0.83 |
| 23 | 204 | 0.11 (0.01) | 0.12 | 0.14 | 55.88 | 0.12 | 0.08 | 0.99 | 0.77 |
| 29 | 470 | 0.15 (0.01) | 0.21 | 0.42 | 62.34 | 0.18 | 0.15 | 0.77 | 0.87 |
| 30 | 406 | 0.15 (0.01) | 0.22 | 0.42 | 63.05 | 0.20 | 0.17 | 0.77 | 0.86 |
| 32 | 462 | 0.15 (0.01) | 0.19 | 0.32 | 61.90 | 0.18 | 0.15 | 0.82 | 0.83 |
| 31 | 286 | 0.14 (0.01) | 0.16 | 0.24 | 55.94 | 0.16 | 0.11 | 0.87 | 0.80 |
| 28 | 381 | 0.12 (0.01) | 0.17 | 0.28 | 68.77 | 0.15 | 0.14 | 0.73 | 0.80 |
| 17 | 19 | 0.22 (0.07) | 0.30 | 0.52 | 52.63 | 0.15 | 0.21 | 0.48 | 0.86 |
| 33 | 109 | 0.16 (0.03) | 0.29 | 0.55 | 65.14 | 0.21 | 0.21 | 0.64 | 0.86 |
| 19 | 367 | 0.08 (0.01) | 0.10 | 0.11 | 73.57 | 0.10 | 0.06 | 0.71 | 0.62 |
| 21 | 17 | 0.13 (0.05) | 0.18 | 0.16 | 64.71 | 0.18 | 0.05 | 0.87 | 0.60 |
| 6 | 47 | 0.08 (0.02) | 0.11 | 0.11 | 74.47 | 0.10 | 0.10 | 0.72 | 0.60 |
| 27 | 131 | 0.22 (0.03) | 0.31 | 0.27 | 50.38 | 0.30 | 0.21 | 0.74 | 0.55 |
| 4 | 248 | 0.07 (0.01) | 0.08 | 0.08 | 77.02 | 0.08 | 0.09 | 0.58 | 0.51 |
| 24 | 59 | 0.16 (0.03) | 0.22 | 0.17 | 52.54 | 0.18 | 0.28 | 0.33 | 0.30 |
| Total | 3901 | 0.04 (0.003) | 0.17 | 0.33 | 66.85 | 0.16 | 0.10 | 0.82 | 0.86 |

[a]*N* represents the total number of daily coincident AOD data, avg is the mean absolute difference between OMI and AERONET, SE is the standard error ($^{SDEV}2 \;/\; \sqrt{N-1}$), SDEV2 is the standard deviation of OMI and AERONET AOD, SDEV1 is the standard deviation of AERONET AOD, and *Q* is the percent of OMI AOD data falling within uncertainty envelope of ±30% or 0.1 AOD from AERONET observations. The results from a linear regression fit are also summarized as the root-mean-square error, the *y* intercept, the slope, and the correlation coefficient ($\rho$).

At sites where AERONET reports measurements at 380 nm, the satellite 388 nm retrieval was directly compared to the 380 nm surface observation. Over those locations where 380 nm measurements are not available, the comparison was made at the shortest available wavelength, generally 440 nm. The OMI 440 nm AOD was obtained by linearly interpolating between the OMAERUV reported 388 and

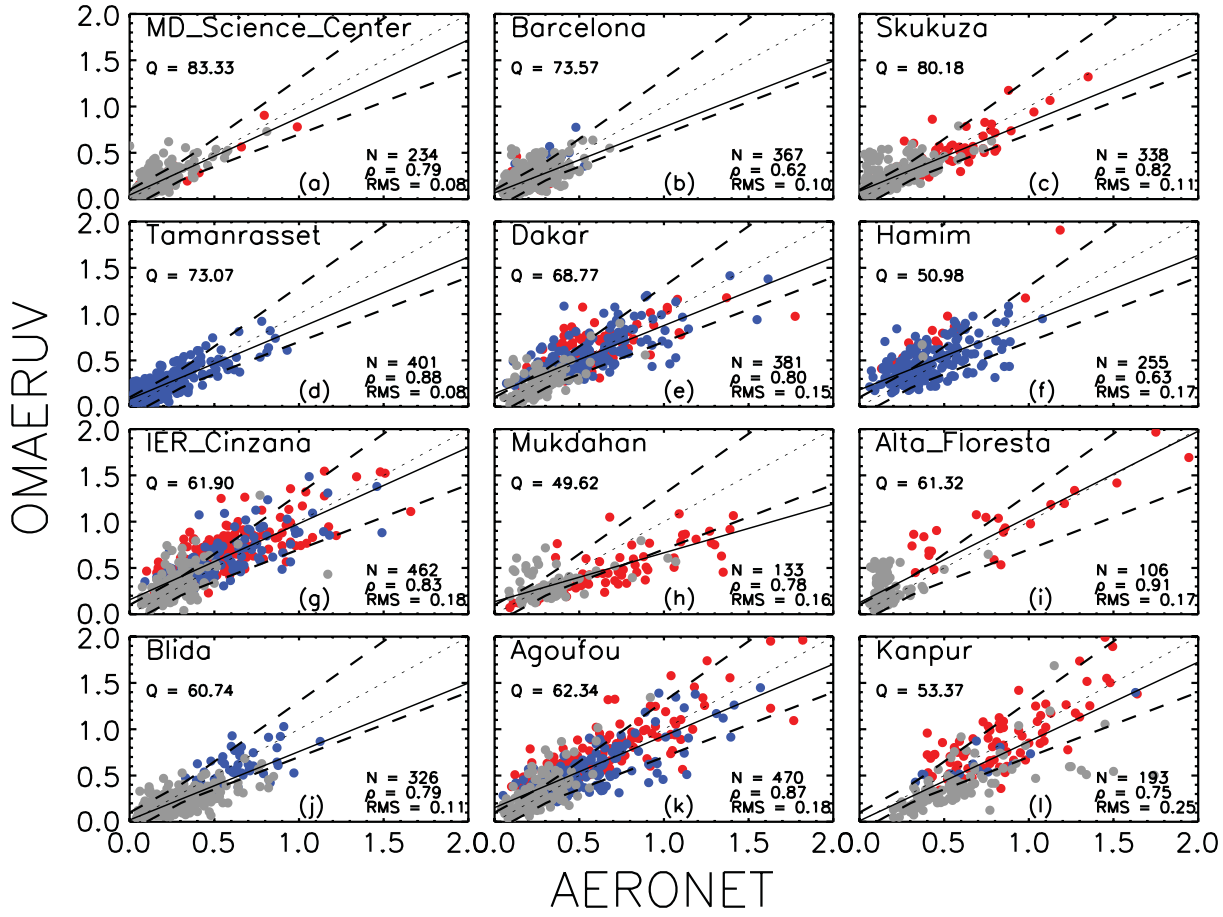


**Figure 4.** AOD comparisons between OMI and AERONET in 2005–2008 at 12 sites. The linear fit is shown as a thick line and the dashed lines indicate the uncertainty envelope of ±30% or 0.1 AOD. The dotted line denotes the 1-to-1 line (see text for details). The colors indicate one of the three predominant aerosol types identified by the OMAERUV algorithm: smoke (red), dust (blue), and urban/industrial (gray).

500 nm values. The AERONET wavelength used for the comparison is listed in Table 1. The OMI AOD retrievals within a radius of 40 km of the AERONET site and within a ±10 min window of the satellite overpass [*Christopher and Wang*, 2004] were averaged after excluding those measurements with standard deviation larger than 0.3 with the purpose of excluding possible remaining cloud contamination effects. The resulting OMI AOD average values are then compared with the time-averaged Sun photometer measurements.

## 3. OMAERUV Validation Analysis

### 3.1. Sensor Stability

The long-term stability of the sensor was examined by analyzing daily OMI-AERONET matchups over the full eight complete years of the OMI sensor operation (2005–2012) at the five AERONET sites. The AOD time series plot (Figure 3a) over the five sites (Goddard Space Flight Center (GSFC), Alta Floresta, Dakar, Institut D'Economie Rural (IER),Cinzana, and XiangHe) for 8 years (2005–2012) shows correlation coefficients between 0.77 and 0.90. In addition, the time series plot (Figure 3b) of the difference of AOD (OMI-AERONET) shows that, although the noise level is high at some locations, no temporal trend is apparent at any of the five sites. This result indicates the absence of any discernible instrumental drift. This analysis supports the conclusion that the method of rejecting the data affected by the row anomaly since 2007 (discussed in section 2.1) successfully removes the faulty measurements without obvious alteration of the quality of the derived product.

### 3.2. Validation Results

Table 2 summarizes the statistics associated with the validation analysis at the 44 AERONET sites in Table 1. In addition to the linear fit statistics (i.e., RMSE, *y* intercept, slope, and correlation coefficient ($\rho$)),

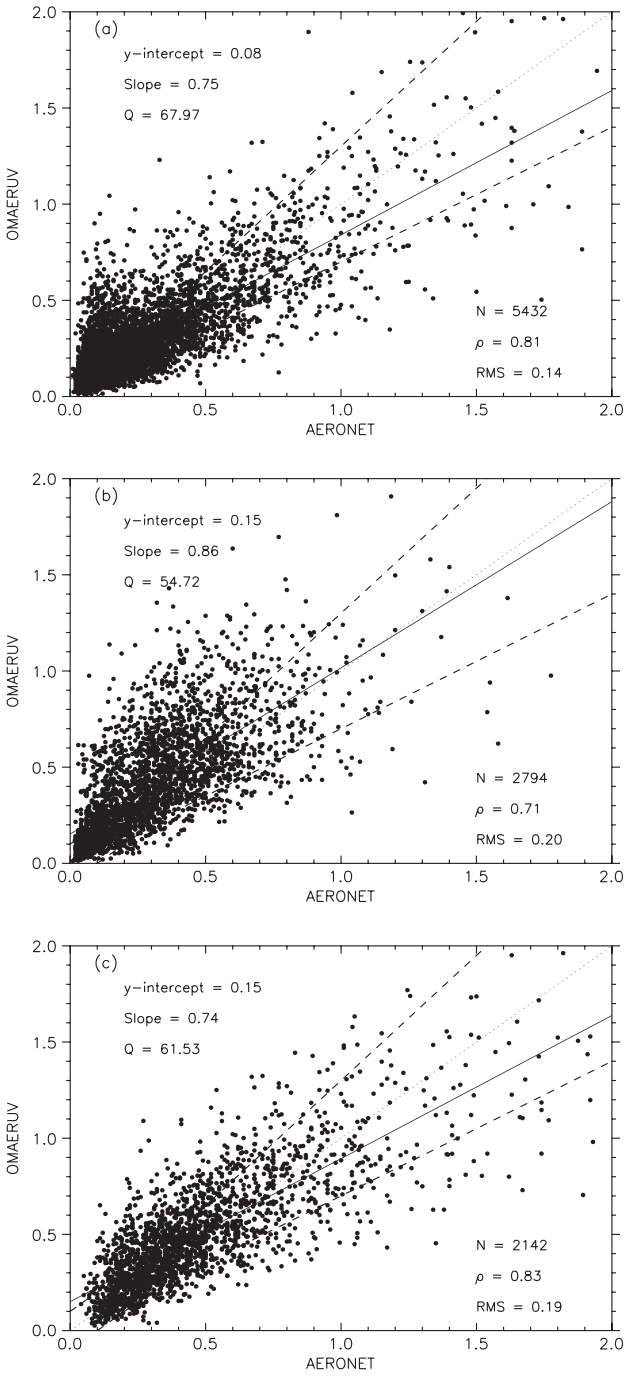


**Figure 5.** AOD comparisons between OMI and AERONET in 2005–2008 at each aerosol type category: (a) nonabsorbing and mixture sites (27), (b) dust sites (10), and (c) smoke sties (7).

the statistical metrics in Table 2 include the mean absolute difference (avg), the standard deviation (SDEV2), the standard error (SE) between OMI and AERONET, and the percent (*Q*) of OMI retrievals within the range of expected uncertainty which is the combined effect of all possible error sources. The combined uncertainty in the derived AOD from the major error sources in the near-UV algorithm (subpixel cloud contamination, aerosol layer height, and surface albedo) is the largest of 0.1 or 30% [*Torres et al.*, 1998, 2002b]. These additional statistics provide an insight of the overall variability of the AOD, and they are less affected by the extreme outliers than the linear fit-derived quantities, especially when the total number of daily pairs (*N*) is small.

To facilitate the discussion, the data in Table 2 are presented in two groups according to the wavelength of the AERONET observation. The top group (28 sites) includes those locations where ground-based observations at 380 nm are available, and therefore, a direct comparison with the satellite observation was possible. The second group (16 stations) lists the sites where 380 nm measurements were not available, and therefore, the OMI AOD was converted to the shortest available AERONET wavelength (generally 440 nm) for the comparison. The tabulated results in both groups have been sorted in terms of the best resulting combination of $\rho$ and slope. The row at the bottom of each tabulation shows the statistics for the two groups of sites. The better statistical metrics of the 440 nm group are a reflection of the more suitable observing conditions (i.e., low subpixel cloud contamination) since most sites in this group are located in arid and semiarid environments. The following discussion of results refers to the totality of the observing sites. Correlation coefficients range between 0.3 and 0.91 with values larger than 0.7 at half of the sites sampled. At eight sites (4, 5, 13, 14, 24, 25, 27, and 37), typically urban and coastal locations, the reported correlation coefficient is lower than 0.6. The main reasons for the low correlation are the combined effect of surface albedo characterization (see discussion below on *y* intercept), cloud contamination, and possibly aerosol model representation.

The resulting slope is lower than unity in all the 44 cases, indicating an overall tendency of the algorithm to underestimate rather than overestimate the atmospheric aerosol load. The *y* intercept of the regression linear fit varies between 0.01 at Site 39 (Kanpur, India) and 0.45 at Site 37 (Dhadnah). Six sites yield values of 0.05 or

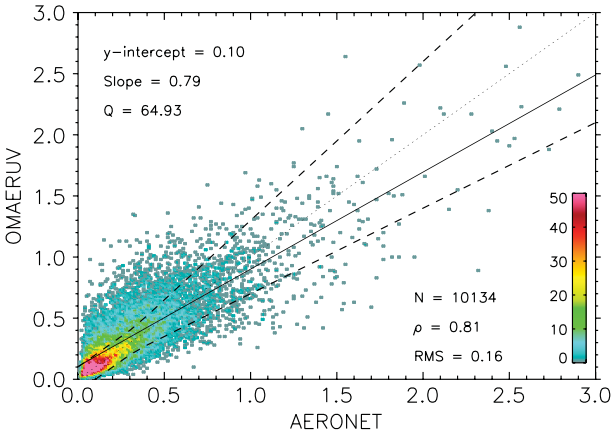


**Figure 6.** Same as the comparison of AOD for individual sites in Figure 4, but for all 44 sites from both OMI and AERONET at 440 nm over 4 years (2005–2008). The color bar represents the number of pairs for each bin with the interval of 0.02 AOD where the minimum number of pairs (1.0) is shown in gray color. The maximum number of pairs between 50 and 110 is shown in pink.

better whereas *y* intercept values larger than 0.15 are reported at 10 sites. At the remaining 28 sites, values between 0.06 and 0.14 were obtained. Large *y* intercept values are associated with inaccurate characterization of surface albedo. The coarse spatial resolution of the climatology of surface albedo (1°×1°) used in OMAERUV may not adequately resolve smaller scale spatial variability of the surface reflective properties in arid regions (Sites 36, 37, and 38) or at typical urban settings such as Mexico City and Cairo (Sites 14 and 24). At coastal sites where the actual surface is a mixture of land and ocean (Sites 13, 25, and 27), the resolution of the surface albedo database may not adequately resolve the surface type at the spatial resolution of the observation.

At 28 out of the 44 locations, the percent of retrievals within the expected uncertainty (*Q*) is 60% or better. Large OMI AOD values beyond the upper limit of +30% uncertainty can be associated with cloud contamination, particularly when the actual AOD is smaller than about 0.3, as shown in Figures 4a, 4b, 4c, 4e, 4h, and 4i, whereas OMI AOD values below the lower limit of −30% uncertainty can be associated with sampling differences, lack of spatial homogeneity of the aerosol load over the large OMI footprint, or inadequacy of the chosen aerosol model. Best statistics ($\rho > 0.75$ and regression line slope between 0.73 and 1.0 and *y* intercepts lower than 0.17) were obtained for 33% of the sites (top seven listings at 380 nm and eight listings at 440 nm in Table 2). Five of these locations (Sites 20, 23, 26, 28, and 29) are located north of 15°N in northern Africa, where the predominant aerosol type is desert dust. The good level of agreement at these desert sites is expected since subpixel cloud contamination, which is the main source of uncertainty of the OMI aerosol products, is expected to be low over arid regions. Also within the top 33%, there are five stations where carbonaceous particles constitute the main contributors to the observed aerosol load (Sites 15, 30, 31,32, and 35) as well as Sites 8, 9,10, and 11, where the aerosol type is dominated by the presence of urban/industrial aerosols. A more detailed discussion of the validation results of the nonabsorbing aerosol type is presented in section 3.3.

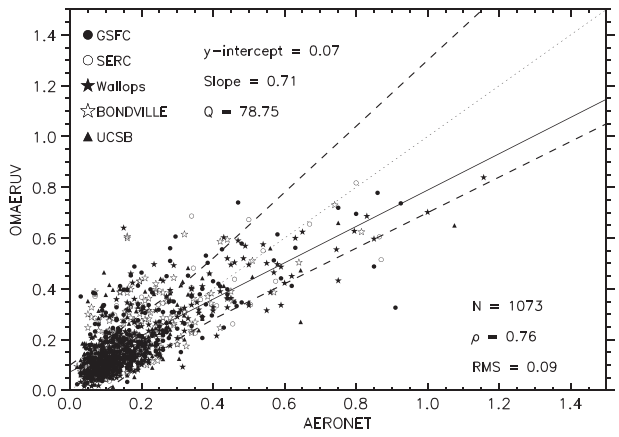


**Figure 7.** OMI (388 nm) and AERONET (380 nm) AOD comparisons at the five selected sites over 4 years (2005–2008). These sites shown as different symbols represent typical nonabsorbing scattering aerosols.

Figure 4 depicts scatterplots of AERONET (*x* axis) and OMAERUV (*y* axis)-measured AOD at a subset of 12 of the 44 stations used in this validation analysis. The obtained linear fit is shown as the thick solid line, and the dashed lines indicate the expected uncertainty envelope of ±30% or 0.1 AOD. The dotted line denotes the 1-to-1 line.

Figure 4 (first row) shows comparisons at Maryland Science Center (NE, USA), Barcelona (Europe), and Skukuza (southern Africa). At these sites, nonabsorbing aerosols are present most of the year. Subpixel cloud contamination is clearly observable at AOD values of 0.3 and lower. At larger AOD values, however, the effect of subpixel cloud contamination does

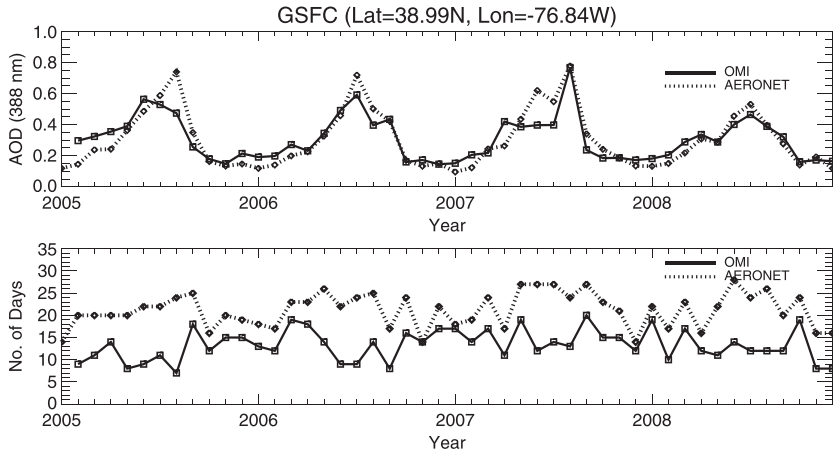


**Figure 8.** Monthly based time series AOD plot at the GSFC site over 4 years.

not appear to be large. Figure 4 (second row) (Tamanrasset, in the Saharan Desert, Dakar, Northwest Africa, and Hamin, Arabian Peninsula) shows comparisons at dust-dominated sites typical of arid and semiarid environments. For this aerosol type, subpixel cloud contamination is very low, and the satellite observations are generally in good agreement with the ground-based measurements. Figure 4 (third row) depicts the OMAERUV-AERONET comparisons at IER, Cinzana (Sahel, North Africa), Mukdahan (Southeast Asia), and Alta Floresta (Amazonia, South America), representatives of regions where carbonaceous aerosols contribute significantly to the aerosol burden during the corresponding biomass burning season.

Figure 4 (fourth row) (Blida, North Africa; Agoufou, Sahel; and Kanpur, northern India) shows comparisons at sites where mixtures of dust and smoke or/and urban pollutants are likely to take place depending on the season. The largest variability in terms of the root-mean-square error (RMSE) (e.g., Kanpur 0.25) is generally observed at these sites. Smoke, dust, and nonabsorbing aerosols are present at different times of the year at Kanpur. The largest optical depth values over Alta Floresta are associated with biomass burning aerosols during the three-monthlong (August to October) biomass burning season, but a small amount of nonabsorbing aerosols are present all year long. A similar situation can be observed at the Dhadnah station ($ID = 37$).

Forty four sites are grouped into three predominant aerosol-type categories (i.e., 27 nonabsorbing and mixture sites, 10 dust sites, and 7 smoke sites) to make scatterplots of statistics in Figure 5. Best statistics ($\rho = 0.81$, RMSE = 0.14, and $Q = 68$) is obtained from the nonabsorbing and mixture group (Figure 5a) for which the possible sources of uncertainty are the cloud contamination and inadequate surface albedo for low AOD values below 0.3. Most of the large variability for large AOD values is very likely due to including the mixture sites (Sites 15, 29, 34, and 39) having dust or smoke-type aerosols for a certain time period as described in section 2.4. Other aerosol groups (i.e., dust and smoke) need an additional assumption of the aerosol layer height in the retrieval which may produce further increased variability (RMSE = 0.20 for dust and RMSE = 0.19 for smoke).

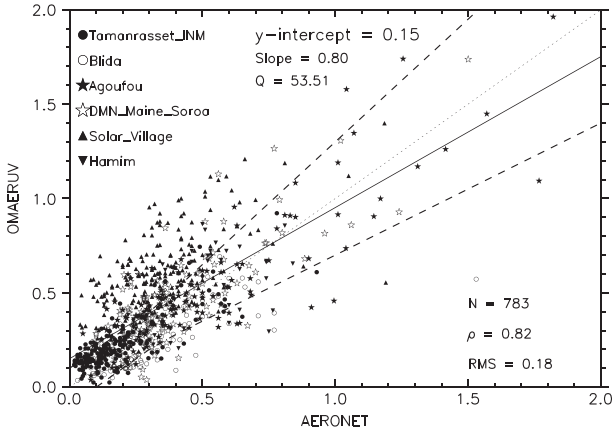


**Figure 9.** AOD comparisons between the OMI (440 nm) and the AERONET (440 nm) at the six dust-dominated sites in 2007.

Figure 6 depicts a global density scatterplot of the OMI-AERONET aerosol optical depth comparison. The plot was produced by binning the data in 0.02 intervals for all the 44 sites. The results of the analysis using the global statistical sample of 10,134 pairs are generally consistent with the best results from the individual sites in Table 2. The global sample yields a satisfactory level of

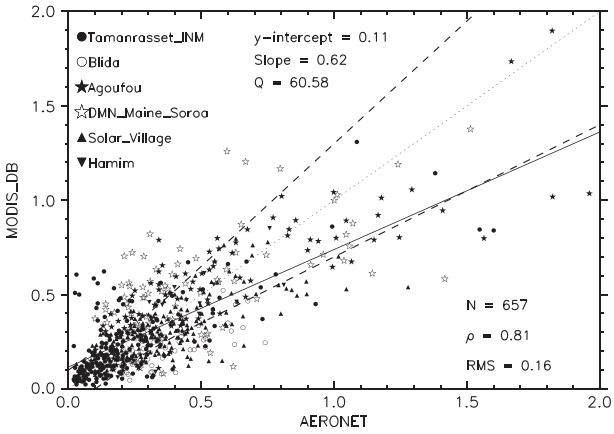


**Figure 10.** Same as Figure 9 but for MODIS DB (440 nm) versus AERONET (440 nm) in 2007. The MODIS DB AOD at 440 nm was linearly interpolated with 412 and 470 nm AOD values of the QA flag 3 (=very good confidence).

agreement between OMI and AERONET ($\rho = 0.81$, RMSE = 0.16, and $Q = 65\%$), indicating possible issues of the surface albedo and cloud contamination in the ranges of low AOD values. Nevertheless, the majority of low OMI AOD data shown as pink colors falls over the dotted 1-to-1 line within the uncertainty envelope of 0.1 AOD. Therefore, cloud contamination may play a more primary role in degrading the statistics than the surface albedo.

### 3.3. Boundary Layer Aerosols

The validation analysis in the previous section focused mainly on the retrieval of carbonaceous and desert dust aerosol plumes that can extend horizontally over thousands of kilometers. Because of the nature of the physical processes driving the emission and atmospheric injection of desert dust (lofting power of soil particles by the wind) and carbonaceous aerosols (strong convection), large amounts of these aerosols downwind from their source regions are often found above the boundary layer. On the other hand, the atmospheric aerosol loading of urban/industrial origin is generally smaller (lower optical depth) than those of smoke and desert dust layers. These optically thinner aerosol plumes are generally contained in the boundary layer, and their horizontal scale is many times smaller than the typical size of carbonaceous and desert dust aerosol clouds. Retrieving AOD of small horizontal-scale plumes using large footprint satellite observations such as OMI is a particularly challenging task as the effect of subpixel cloud contamination can significantly reduce the retrieval yield and produce an overestimate of the aerosol load [*Remer et al.*, 2012]. For cloud-free conditions, optical depth underestimation may take place when the horizontal scale of the aerosol plume is significantly smaller than the satellite footprint. Under those conditions, the aerosol signal is smeared over the large pixel area yielding a lower optical depth than would be measured at the ground or by a finer resolution satellite-borne sensor.

A comparison of OMAERUV retrieved to AERONET-measured AOD at a subset of sites in Table 1 is depicted in Figure 7. At these five sites in the continental United States (GSFC, Sustainable Environment Research Center (SERC), Wallops, Bondville, and University of California Santa Barbara (UCSB)), the aerosol loading is typically associated with background urban/industrial particles near the surface. The validation analysis of the combined data set yields a correlation coefficient of 0.76, a slope of 0.71, and 0.07 as *y* intercept. The effect of subpixel cloud contamination is clearly observable as the cluster of retrieved values associated with AERONET measurements of AOD 0.3 and lower. At larger AOD values, the incidence of overestimates (most likely due to subpixel cloud effects) goes down rapidly. The average frequency of retrieval days per year over these five sites is 15% (from Table 2), which represents less than half the OMAERUV retrieval frequency over desert areas.

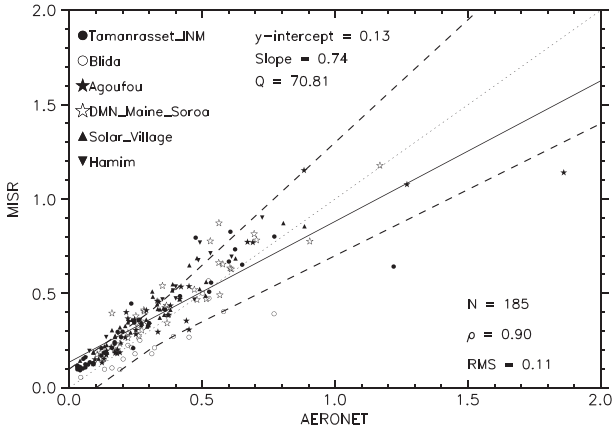


**Figure 11.** Same as Figure 9 but for MISR (446 nm) versus AERONET (440 nm) in 2007. The MISR AOD values with the QA flags 0 and 1 (=successful aerosol mixtures) were used.

The representativeness of OMAERUV temporal averages of AOD based on cloud-contamination-induced reduced sampling can be evaluated by comparing the monthly average satellite

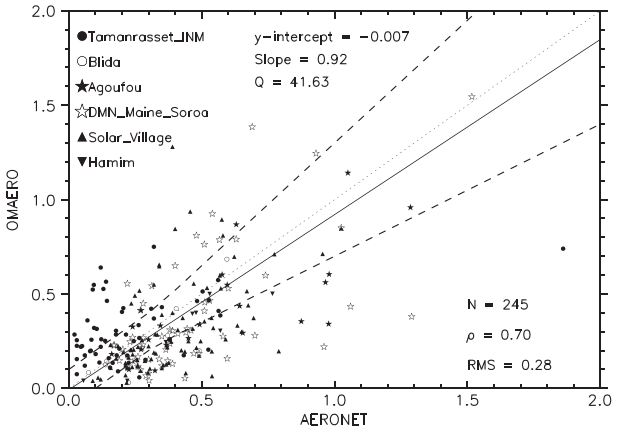


**Figure 12.** Same as Figure 9 but for OMAERO (442 nm) versus AERONET (440 nm) in 2007. Note that QA flags are not available from the OMI-KNMI algorithm.

measurement to AERONET monthly AOD values at the satellite overpass time. Figure 8 (top) showing such a comparison at the GSFC site for the 4 year period in this analysis indicates a close agreement between the two data sets. Figure 8 (bottom) depicts the number of days per month available for calculating the monthly average. Overall, the OMAERUV long-term record closely tracks the AERONET time series. The preceding analysis clearly shows the sensitivity of near-UV observations to the total aerosol column down to the surface. The comparison after 2008 (not shown) shows the clear effect of the row anomaly issue as the satellite sampling is significantly reduced.

## 4. Comparison to Other Satellite Data Sets

In this section, an evaluation of OMAERUV AOD product is carried out by comparison to similar satellite data sets. The direct intercomparison of satellite AOD products is generally a complicated problem due to several reasons including temporal collocation of the data sets, reporting wavelength, and specific algorithmic issues such as cloud masking and aerosol model representation. These issues make it very difficult to understand the reasons for the observed differences in a direct sensor-to-sensor comparison. In this analysis, we have carried out an indirect evaluation of OMAERUV's AOD retrieval capability over bright surfaces with respect to the retrieval results of other algorithms using observations of sensors with similar capability such as MISR [*Kahn et al*., 2009], MODIS Deep Blue algorithm [*Hsu et al*., 2004], and KNMI's OMAERO algorithm [*Torres et al*., 2007]. The retrieval results by the four algorithms during the same period and at the same locations are independently compared to AERONET AOD measurements. Comparisons are carried out for year 2007 at six AERONET sites in Table 1 (*ID* = 20, 26, 29, 31, 36, and 38), four of which are in northern Africa, one in the United Arab Emirates (Hamim), and one in Saudi Arabia (Solar Village).

Figures 9 to 12 show comparisons of AERONET observations to satellite retrievals of AOD derived by the OMAERUV, MODIS DB, MISR, and OMAERO algorithms, respectively, at the six selected sites. All observations available during 2007 were included in the analysis, and the spatial-temporal collocation with the

**Table 3.** Summary Statistics of AOD Comparisons Among Instruments Against AERONET in 2007[a]

| Site | Tamanrassett | | | | Blida | | | | Agoufou | | | |
|---|---|---|---|---|---|---|---|---|---|---|---|---|
| Data Set | OMN | MDB | MSR | OMK | OMN | MDB | MSR | OMK | OMN | MDB | MSR | OMK |
| *N* | 177 | 191 | 42 | 60 | 86 | 51 | 20 | 11 | 141 | 97 | 35 | 24 |
| $\rho$ | 0.90 | 0.73 | 0.89 | 0.79 | 0.77 | 0.76 | 0.86 | 0.82 | 0.94 | 0.87 | 0.94 | 0.79 |
| Slope | 0.77 | 0.61 | 0.78 | 1.09 | 0.53 | 0.49 | 0.66 | 0.94 | 0.81 | 0.56 | 0.64 | 1.30 |
| *y* intercept | 0.08 | 0.09 | 0.11 | 0.07 | 0.06 | 0.02 | 0.03 | −0.05 | 0.11 | 0.22 | 0.15 | −0.25 |
| RMSE | 0.08 | 0.14 | 0.10 | 0.32 | 0.10 | 0.07 | 0.07 | 0.10 | 0.16 | 0.18 | 0.12 | 0.39 |
| Site | DMN Maine Soroa | | | | Solar Village | | | | Hamin | | | |
| Data Set | OMN | MDB | MSR | OMK | OMN | MDB | MSR | OMK | OMN | MDB | MSR | OMK |
| *N* | 122 | 77 | 33 | 59 | 204 | 220 | 41 | 82 | 53 | 21 | 14 | 9 |
| $\rho$ | 0.79 | 0.70 | 0.93 | 0.61 | 0.62 | 0.74 | 0.95 | 0.51 | 0.59 | 0.80 | 0.95 | 0.89 |
| Slope | 0.89 | 0.57 | 0.91 | 0.72 | 0.73 | 0.48 | 0.92 | 0.68 | 0.59 | 0.82 | 1.07 | 0.75 |
| *y* intercept | 0.10 | 0.27 | 0.10 | 0.04 | 0.34 | 0.13 | 0.11 | 0.04 | 0.21 | 0.04 | 0.10 | −0.02 |
| RMSE | 0.16 | 0.22 | 0.08 | 0.25 | 0.17 | 0.10 | 0.05 | 0.21 | 0.16 | 0.11 | 0.06 | 0.07 |

[a]Listed parameters are the total number of pairs (*N*), linear fit statistics (i.e., $\rho$, slope, *y* intercept, and RMSE) for each AOD satellite data sets (OMN: OMAERUV, MDB: MODIS DB, MSR: MISR, and OMK: OMAERO) at six AERONET sites.

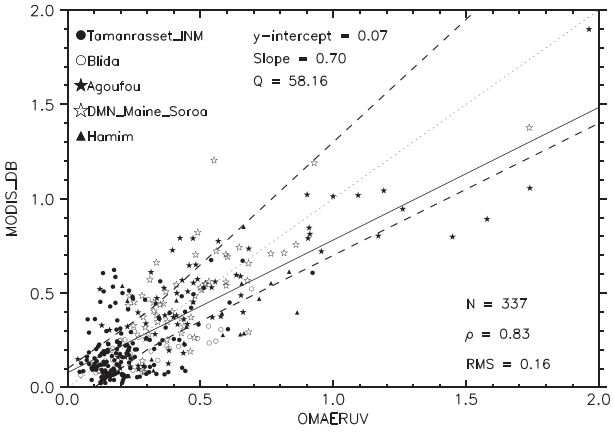


**Figure 13.** Same as Figure 9 but for MODIS DB (440 nm) versus OMAERUV (440 nm) in 2007. Coincident AOD pairs between MODIS DB and OMI were based on the same days (*N*) with respect to AERONET AOD in Figures 9 and 10.

ground-based observations was done using the same procedure outlined in section 2.4. A summary of the resulting statistics is shown in Table 3.

The OMAERUV results in Figure 9 and Table 3 are consistent with the analysis in section 3. As a consequence of the reduced number of points, however, the reported statistics are slightly different. At the Solar Village site, a clear bias between the OMAERUV and the observed ground-based observations are likely associated with inadequate representation of surface reflective properties. The large *y* intercept (0.34) seems to indicate a large underestimation in the assumed surface albedo. Most of the overestimated AOD values in Figure 9 correspond to the measurements at this site.

Figure 10 and Table 3 show MODIS DB-AERONET AOD comparisons. In general, OMAERUV retrievals correlate better than MODIS DB with AERONET measurements except at the Solar Village and Hamin sites. At these two sites, MODIS DB also reports lower *y* intercept values than OMAERUV. MODIS DB slopes at the Agoufou, and DMN Maine Soroa locations (0.56 and 0.57) are significantly lower than those yielded by OMAERUV (0.81 and 0.89).

The MISR-AERONET comparison in Figure 11 and Table 3 shows overall good agreement with the ground-based observations. Issues associated with overestimates at low AOD values and underestimates at high AOD values have been documented [*Kahn et al.*, 2010]. The MISR-AERONET correlation coefficients are slightly better than those of the OMAERUV-AERONET analysis except at the Solar Village and Hamim sites where OMAERUV coefficients are significantly lower. The MISR and OMAERUV reported slopes are comparable at five sites out of six sites. At the Hamim station, the MISR slope is very close to unity as compared to the OMI slope value of 0.72. The MISR and OMAERUV *y* intercepts are comparable at all sites but Solar Village.

Scatterplots of the AERONET-OMAERO comparisons at six locations are shown in Figure 12, and the statistics of the analysis are listed in Table 3. Unlike the other three products in the analysis, the OMAERO aerosol product does not provide a qualifier of the accuracy of the retrievals that could be used to reject unreliable retrievals due to subpixel cloud contamination or other error sources. The combined number of OMAERO-AERONET pairs at the six sites (245) is only about 30% of the OMAERUV-AERONET pairs (783). This is very surprising since both algorithms are applied to the same OMI observations, and the effects of subpixel cloud contamination are expected to be very small over the arid environment characteristic of these AERONET sites. The OMAERO reports correlation coefficients similar to OMAERUV at four of the sites. The much larger OMAERO RMSE values than those obtained by the comparisons with the other three sensors point to systematic retrieval errors possibly associated with aerosol-type identification. The need to simultaneously account for aerosol plume height, aerosol type, and optical depth effects on the measured reflectances leads to large variability in the retrieved AOD.

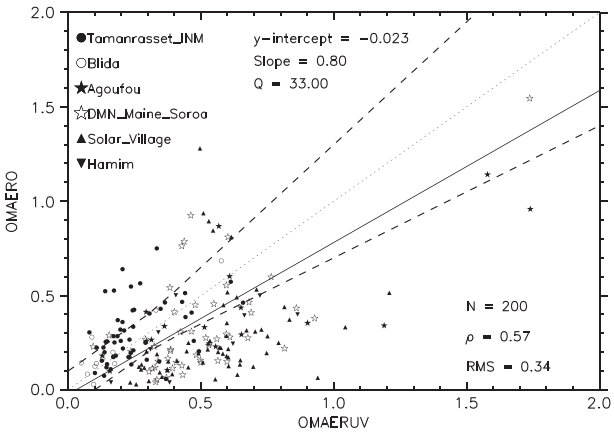


**Figure 14.** Same as Figure 9 but for OMAERO (442 nm) versus OMAERUV (440 nm) in 2007. Coincident AOD pairs between KNMI and OMAERUV were based on the same days (*N*) with respect to AERONET AOD in Figures 9 and 12.

Since the OMAERO and MODIS DB retrievals are also obtained from A-train sensors, it is actually possible to generate scatterplots of space and time-collocated measurements of these products and the OMAERUV. Because of the significant time difference in observation time (about 3 h), a direct MISR-OMAERUV comparison has not been attempted.

The MODIS DB-OMAERUV comparison is presented in Figure 13. Although this analysis was made assuming no time difference between the daily OMI and MODIS observations, the actual overpass time difference between the Aqua and Aura satellites is about 8 min. The intercomparison yields a 0.83 correlation coefficient, a 0.07 *y* intercept, and a 0.70 slope. Because of the previously discussed OMAERUV bias at the Solar Village site, observations at this AERONET station are not included in Figure 13.

The comparison of OMAERUV and OMAERO AOD retrievals is shown in Figure 14. Because these two products are developed from observations by the same sensor, exact spatial and temporal collocation is automatically achieved. The comparison was done using retrievals by the two algorithms on the pixels deemed reliable by OMAERUV quality flagging because OMAERO does not provide retrieval quality information. A large degree of scatter is apparent, and the resulting correlation coefficient is 0.57 and the *y* intercept and slope of the regression fit are −0.02 and 0.80, respectively. The large observed discrepancy can only be explained in terms of algorithmic differences since issues associated with subpixel cloud contamination and pixel size are common to both products. The OMAERUV AOD retrievals show comparable levels of agreement with ground-based observations as those resulting from the validation analysis of MODIS DB and MISR measurements especially over desert and biomass burning dominant regions.

## 5. Summary and Conclusions

Aerosol optical depth data reprocessed with the OMI UV aerosol algorithm (version 1.4.2) have been assessed by comparing to AERONET direct Sun measurements. A comparison over 8 years (2005–2012) at five AERONET locations shows no sign of degradation in OMI's radiometric calibration in the near UV. This is an encouraging finding given the uncertainty associated with the effect of the row anomaly issue that has, since 2007, reduced by half the sensor's viewing capability. The lack of any identifiable trend in the measured record indicates that the exclusion procedure accurately removed the affected data.

A rigorous AOD validation analysis over 4 years (2005–2008) was carried out. The OMAERUV and AERONET AOD observations were compared at 44 globally distributed sites representative of the most commonly observed aerosol types. A detailed statistical analysis of the validation analysis is summarized in Table 2. In general, the algorithm performance is best over sites situated not too far from the source areas of desert and carbonaceous aerosols. These large-scale aerosol events generally take place primarily under cloud-free conditions that facilitate the retrieval. On the other hand, small-scale wind-blown aerosol plumes are commonly found in the vicinity of clouds over island sites and coastal areas. Under these dynamic meteorological conditions, aerosols and clouds can be highly variable within the large OMI footprint. As a consequence, the conditions for successful retrievals are scarce, and therefore, both retrieval yield and quality are diminished. The overall performance of the retrieval algorithm over the totality of the sites yields an RMSE of 0.16 and a correlation coefficient of 0.81. The percent of OMAERUV AOD retrievals within the expected uncertainty range is 65%.

The validation analysis presented here also shows that near-UV measurements can be successfully used not only for retrieving the AOD of lofted layers of carbonaceous and desert dust particles but also for retrieving the AOD of boundary layer aerosols above vegetated land. The OMI-AERONET AOD comparison for boundary layer aerosols shows that the near-UV observations are sensitive to aerosol presence all the way down to the bottom of the atmospheric column.

The accuracy of OMI AOD retrieval was further evaluated relative to those of similar satellite products by simultaneously comparing OMAERUV, MODIS DB, MISR, and OMAERO retrievals to AERONET observations in 2007 at a subset of stations in northern Africa characterized by bright surfaces and minimum subpixel cloud contamination. The results confirmed that for cloud-free conditions over arid and semiarid environments, OMAERUV accuracy is comparable to those from the MODIS DB and MISR algorithms that make use of fine resolution observations.

The AOD validation analysis presented here, in conjunction with the forthcoming paper on SSA evaluation (Jethva et al., Global assessment of OMI aerosol single-scattering albedo in relation to ground-based

AERONET inversion, submitted to *Journal of Geophysical Research*, 2014), constitutes the most comprehensive assessment to date of the aerosol products generated by the OMI OMAERUV algorithm. In spite of the inherent retrieval difficulties associated with the coarse spatial resolution of the measurements, the OMAERUV data set containing aerosol optical depth and single-scattering albedo is an important contribution to the observational database available for improving our current understanding of the role of the of the global aerosol loading in the energy balance of the earth-atmosphere system. The OMAERUV provides a complementary record on aerosol optical depth over land areas, especially over arid and semiarid regions.

This analysis confirms the large potential of using near-UV observations as a powerful remote sensing tool for AOD retrieval over land. Its main advantage is the low-UV surface albedo that allows aerosol detection without requiring multiple-angle viewing or additional spectral measurements for accurate characterization of surface effects. The addition of near-UV channels in future high-spatial-resolution aerosol sensing missions is therefore strongly recommended.

**Acknowledgments**

We thank the NASA data centers listed in section 2 for providing AOD data from OMI, MODIS, and MISR sensors. We also thank the AERONET principal investigators for their efforts in establishing and maintaining the sites that make it possible to evaluate satellite AOD values in this intercomparison study. Useful comments and suggestions from Lorraine Remer and the two anonymous reviewers to improve the quality of this paper are also acknowledged. This work was performed under contract with NASA.

## References

Ahn, C., O. Torres, and P. K. Bhartia (2008), Comparison of OMI UV Aerosol Products with Aqua-MODIS and MISR observations in 2006, *J. Geophys. Res.*, *113*, D16S27, doi:10.1029/2007JD008832.

Al-Saadi, J., et al. (2005), Improving national air quality forecasts with satellite aerosol observations, *Bull. Am. Meteorol. Soc.*, *86*(9), 1249–1261.

Christopher, S. A., and J. Wang (2004), Intercomparison between multi-angle imaging spectroradiometer (MISR) and sunphotometer aerosol optical thickness in dust source regions over China: Implications for satellite aerosol retrievals and radiative forcing calculations, *Tellus*, *56B*, 451–456.

Chu, D. A., Y. J. Kaufman, C. Ichoku, L. A. Lemer, D. Tanré, and B. N. Holben (2002), Validation of MODIS aerosol optical depth retrieval over land, *Geophys. Res. Lett.*, *29*(12), 8007, doi:10.1029/2001GL013205.

Deuzé, J. L., et al. (2001), Remote sensing of aerosols over land surfaces from POLDER-ADEOS-1 polarized measurements, *J. Geophys. Res.*, *106*, 4913–4926.

Diner, D. J., J. V. Martonchik, R. A. Kahn, B. Pinty, N. Gobron, D. L. Nelson, and B. N. Holben (2005), Using angular and spectral shape similarity constraints to improve MISR aerosol and surface retrievals over land, *Remote Sens. Environ.*, *94*, 155–171.

Dobber, M., et al. (2008), Validation of Ozone Monitoring Instrument level-1b data products, *J. Geophys. Res.*, *113*, D15S06, doi:10.1029/2007JD008665.

Holben, B. N., et al. (1998), AERONET—A federated instrument network and data archive for aerosol characterization, *Remote Sens. Environ.*, *66*, 1–16.

Hsu, N. C., S. C. Tsay, M. D. King, and J. R. Herman (2004), Aerosol properties over bright-reflecting source regions, *IEEE Trans. Geosci. Remote Sens.*, *42*, 557–569.

Jethva, H., and O. Torres (2011), Satellite-based evidence of wavelength-dependent aerosol absorption in biomass burning smoke inferred from Ozone Monitoring Instrument, *Atmos. Chem. Phys.*, *11*, 10,541–10,551.

Kahn, R. A., et al. (2009), MISR aerosol product attributes and statistical comparisons with MODIS, *IEEE Trans. Geosci. Remote Sens*, *47*(12, Part 2), 4095–4114.

Kahn, R., B. J. Gaitley, M. J. Garay, D. J. Diner, T. F. Eck, A. Smirnov, and B. N. Holben (2010), Multiangle Imaging SpectroRadiometer global aerosol product assessment by comparison with the Aerosol Robotic Network, *J. Geophys. Res.*, *115*, D23209, doi:10.1029/2010JD014601.

Kaufman, Y. J., D. Tanre, L. A. Lemer, E. F. Vermote, A. Chu, and B. N. Holben (1997), Operational remote sensing of tropospheric aerosol over land from EOS moderate resolution imaging spectrometer, *J. Geophys. Res.*, *102*, 17,051–17,067.

King, M. D., Y. J. Kaufman, D. Tanre, and T. Nakajima (1999), Remote sensing of tropospheric aerosols from space: Past, present and future, *Bull. Am. Meteorol. Soc.*, *80*, 2229–2259.

Kinne, S., et al. (2006), An AeroCom initial assessment - Optical properties in aerosol component modules of global models, *Atmos. Chem. Phys.*, *6*, 1815–1834.

Leitão, J., A. Richter, M. Vrekoussis, A. Kokhanovsky, Q. J. Zhang, M. Beekmann, and J. P. Burrows (2010), On the improvement of $NO_2$ satellite retrievals – Aerosol impact on the airmass factors, *Atmos. Meas. Tech.*, *3*, 475–493.

Levelt, P. F., E. Hilsenrath, G. W. Leppelmeier, G. H. J. van den Oord, P. K. Bhartia, J. Taminnen, J. F. de Haan, and J. P. Veefkind (2006), Science objectives of the Ozone Monitoring Instrument, *IEEE Trans. Geosci. Remote Sens.*, Special Issue of the EOS-Aura mission, *44*(5), 1093–1101.

Levy, R. C., L. A. Remer, R. G. Kleidman, S. Mattoo, C. Ichoku, R. Kahn, and T. F. Eck (2010), Global evaluation of the Collection 5 MODIS dark-target aerosol products over land, *Atmos. Chem. Phys.*, *10*, 10,399–10,420, doi:10.5194/acp-10-10399-2010.

Martonchik, J. V., D. J. Diner, R. Kahn, M. M. Verstraete, B. Pinty, H. R. Gordon, and T. P. Ackerman (1998), Techniques for the retrieval of aerosol properties over land and ocean using multiangle imaging, *IEEE Trans. Geosci. Remote Sens.*, *36*, 1212–1227.

Remer, L. A., S. Mattoo, R. C. Levy, A. Heidinger, R. B. Pierce, and M. Chin (2012), Retrieving aerosol in a cloudy environment: aerosol availability as a function of spatial and temporal resolution, *Atmos. Meas. Tech. Discuss.*, *5*, 627–662.

Ridley, D. A., C. L. Heald, and B. Ford (2012), North African dust export and deposition: A satellite and model perspective, *J. Geophys. Res.*, *117*, D02202, doi:10.1029/2011JD016794.

Schoeberl, M. R., et al. (2006), Overview of the EOS Aura Mission, *IEEE Trans. Geosci. Remote Sens.*, *44*(5), 1066–1074.

Stephens, G. L., et al. (2002), The Cloudsat mission and the A-train – A new dimension of space-based observations of clouds and precipitation, *Bull. Am. Meteorol. Soc.*, *83*(12), 1771–1790.

Torres, O., P. K. Bhartia, J. R. Herman, and Z. Ahmad (1998), Derivation of aerosol properties from satellite measurements of backscattered ultraviolet radiation: Theoretical Basis, *J. Geophys. Res.*, *103*, 17,099–17,110.

Torres, O., P. K. Bhartia, J. R. Herman, A. Syniuk, P. Ginoux, and B. N. Holben (2002a), A long-term record of aerosol optical depth from TOMS observations and comparison to AERONET measurements, *J. Atmos. Sci.*, *59*, 398–413.

Torres, O., R. Decae, J. P. Veefkind, and G. de Leeuw (2002b), OMI aerosol retrieval algorithm, in *OMI Algorithm Theoretical Basis Document: Clouds, Aerosols, and Surface UV Irradiance*, vol. 3, version 2, OMIATBD-03, edited by P. Stammes, pp. 47–71, NASA Goddard Space Flight Cent., Greenbelt, Md. [Available at http://eospso.gsfc.nasa.gov/eos_homepage/for_scientists/atbd/docs/OMI/ATBD-OMI-03.pdf.]

Torres, O., A. Tanskanen, B. Veihelmann, C. Ahn, R. Braak, P. K. Bhartia, P. Veefkind, and P. Levelt (2007), Aerosols and surface UV products from Ozone Monitoring Instrument observations: An overview, *J. Geophys. Res.*, *112*, D24S47, doi:10.1029/2007JD008809.

Torres, O., C. Ahn, and Z. Chen (2013), Improvements to the OMI near UV Aerosol Algorithm using A-train CALIOP and AIRS observations, *Atmos. Meas. Tech.*, *6*, 5621–5652, doi:10.5194/amtd-6-5621-2013.

van Donkelaar, A., R. V. Martin, M. Brauer, R. Kahn, R. Levy, C. Verduzco, and P. Villeneuve (2010), Global estimates of average ground-level fine particulate matter concentrations from satellite-based aerosol optical depth, *Environ. Health Perspect.*, *118*, 847–855.

Wang, J., and S. A. Christopher (2003), Intercomparison between satellite-derived aerosol optical thickness and PM2.5 mass: Implication for air quality studies, *Geophys. Res. Lett.*, *30*(21), 2095, doi:10.1029/2003GL018174.

Winker, D. M., et al. (2006), The CALIPSO mission and initial results from CALIOP, *Proc. SPIE*, *6409*, 640,902, doi:10.1117/12.698003.

Xu, X., J. Wang, D. Henze, W. Qu, and M. Kopacz (2013), Constraints on aerosol sources using GEOS-Chem adjoint and MODIS radiances, and evaluation with Multi-sensor (OMI, MISR) data, *J. Geophys. Res. Atmos.*, *118*, 6396–6413, doi:10.1002/jgrd.50515.

Zhang, J., and S. Christopher (2003), Longwave radiative forcing of Saharan dust aerosols estimated from MODIS, MISR, and CERES observations on Terra, *Geophys. Res. Lett.*, *30*(23), 2188, doi:10.1029/2003GL018479.

Zhang, J., J. S. Reid, D. Westphal, N. Baker, and E. J. Hyer (2008), A system for operational aerosol optical depth data assimilation over global oceans, *J. Geophys. Res.*, *113*, D10208, doi:10.1029/2007JD009065.